— Report —

The effective use of shortwave penetration below the ocean surface in a MOM3-based ocean general circulation model

Nobumasa Komori[1*], Bunmei Taguchi[1], and Hideharu Sasaki[1]

There are two problems with the shortwave penetration scheme used in Modular Ocean Model version 3 (MOM3): (i) the spatiotemporal variability of the thickness of the first layer resulting from the free surface is not considered, and (ii) shortwave irradiance penetrates the ocean bottom. Because both of these problems can cause artificial heat sources or sinks, their effects are evaluated in the present study using a MOM3-based ocean general circulation model. The first problem creates an artificial heat sink (source) in the regions of positive (negative) sea surface height (SSH) with a maximum amplitude greater than 10 W m^{-2} and decreases (increases) sea surface temperature (SST) by up to $0.3\,°\text{C}$ on the basis of annual mean. This change in SST leads to a reduction in global mean evaporation and, as a result, an increase in SSH, which enhances the artificial heat sink. After several years of integration, this positive feedback amplifies the effects of the first problem in cases of stand-alone ocean simulations forced by freshwater flux. The estimated artificial heat sink induced by the second problem reaches 50 W m^{-2}, and the decrease in SST exceeds $1.0\,°\text{C}$. However, the effects of this problem are restricted within shallow coastal areas and do not involve positive feedback.

---

1   Earth Simulator Center (ESC), Japan Agency for Marine-Earth Science and Technology (JAMSTEC)

*Corresponding author:

   Nobumasa Komori

   Earth Simulator Center (ESC), Japan Agency for Marine-Earth Science and Technology (JAMSTEC)

   3173-25 Showa-machi, Kanazawa-ku, Yokohama 236-0001, Japan

   Tel. +81-45-778-5844

   komori@jamstec.go.jp

1. Introduction

The Geophysical Fluid Simulation Research Group at the Earth Simulator Center of JAMSTEC develops and maintains an ocean general circulation model (OGCM) for high-resolution simulation study of the ocean on the Earth Simulator in collaboration with researchers at the Research Institute for Global Change of JAMSTEC. The model, the OGCM for the Earth Simulator (OFES; Masumoto et al., 2004), is based on Modular Ocean Model version 3 (MOM3; Pacanowski and Griffies, 1999), which is a z-coordinate model with a free surface and a partial bottom cell and was developed at the Geophysical Fluid Dynamics Laboratory of NOAA.

In ocean simulations with a vertical layer thickness of several to ten meters at the surface, it is well known that the penetration of a portion of the shortwave irradiance entering the ocean into the deeper layers must be accounted for to avoid an excess heating of the first layer in the model. This function of "shortwave penetration" is incorporated in MOM3. However, there are deficiencies in the numerical treatment of this effect, which can result in the modeling of an artificial heat source/sink. Shortwave irradiance is a primary energy source of the general circulation of the ocean, and its appropriate treatment in OGCM is crucial for realistic ocean simulations and for coupled atmosphere–ocean simulations.

In this report, we describe two problems with the original shortwave penetration scheme used in MOM3; propose a modified algorithm for MOM3 and MOM3-based OGCMs, including OFES; and evaluate the effects of these problems through experimental simulations using OFES. Although a newer version of MOM (MOM4; Griffies et al., 2004; Griffies, 2007) has been released and the problems seem to be fixed, MOM3 is still in wide use, and this report may be helpful to users of MOM3.

2. Shortwave penetration scheme

2.1. Original scheme

We briefly describe the shortwave penetration scheme used in MOM3. For details, refer to the MOM3 manual (Pacanowski and Griffies, 1999, in particular, section 28.2.10). The notation follows the manual, and the schematics of the vertical coordinate system are depicted in Fig. 1.

According to Paulson and Simpson (1977), the shortwave penetration ratio pen_k at the bottom of the vertical k-th cell is expressed as the sum of two exponential functions of its depth zw_k from a fixed reference surface level ($z = 0$):

$$pen_k = A \cdot e^{-zw_k/l_1} + (1-A) \cdot e^{-zw_k/l_2} \quad (k = 1,..., km), \qquad (1)$$

where A = 0.58; $l_1 = 0.35$ m and $l_2 = 23.0$ m are attenuation lengths for longer and shorter wavelengths, respectively, and the values are for the case of water Type I (clear water; Jerlov, 1976). The vertical profile of the ratio is shown in Fig. 2 (black line). The divergence of penetration ratio is calculated as

$$divpen_k = \frac{pen_{k-1} - pen_k}{dzt_k} \quad (k = 1,..., km), \qquad (2)$$

where $dzt_k = zw_k - zw_{k-1}$ is the thickness of the k-th cell ($zw_0 = 0$). In the prognostic equation, the subsurface temperature change resulting from the divergence is added to an internal source term $source_{i,k,j}$ given by

$$source_{i,k,j} = source_{i,k,j} + sbcocn_{i,j,isw} \cdot divpen_k \qquad (3)$$

where $sbcocn_{i,j,isw}$ is the shortwave surface boundary condition at the horizontal grid point of (i, j). Because surface net heat flux $stf_{i,j,1}$, which is the surface boundary condition for vertical diffusion, already includes a shortwave component, the penetration ratio at the surface is set to zero ($pen_0 = 0$) to prevent the shortwave component from being added in twice.
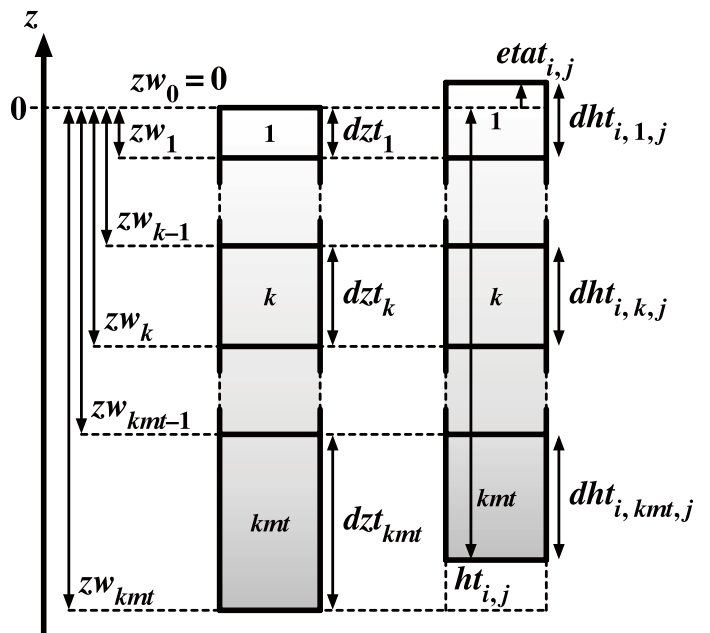

Fig. 1. Schematics of the vertical coordinate system used in MOM3. See the text for definitions of the variables. Two-headed arrows represent positive quantities. Note that the subscription k increases with depth, whereas the vertical coordinate z is upwardly positive.

When the free surface and/or partial bottom cell are considered, the layer thickness dzt_k is replaced by $dht_{i,k,j}$ as

$$dht_{i,k,j} = \begin{cases} zw_1 + etat_{i,j} = dzt_1 + etat_{i,j} & (k=1) \\ zw_k - zw_{k-1} = dzt_k & (k=2,...,kmt_{i,j}-1) \\ ht_{i,j} - zw_{kmt_{i,j}-1} & (k=kmt_{i,j}) \end{cases} \quad (4)$$

where $etat_{i,j}$ is sea surface height (SSH), $ht_{i,j}$ is the ocean depth, and $kmt_{i,j}$ is number of ocean cells in the vertical direction (Fig. 1). The replacement is true except for Eq. (2), and $divpen_k$ is calculated once at the beginning of the integration and does not change horizontally or temporally.

2.2. Problems and modifications

Integrating the second term in the r.h.s. of Eq. (3) from surface ($k=1$) to bottom ($k=kmt_{i,j}$) cells yields the following:

$$\sum_{k=1}^{kmt_{i,j}} sbcocn_{i,j,isw} \cdot divpen_k \cdot dht_{i,k,j}$$

$$= sbcocn_{i,j,isw} \sum_{k=1}^{kmt_{i,j}} (pen_{k-1} - pen_k) \cdot \frac{dht_{i,k,j}}{dzt_k}$$

$$= -sbcocn_{i,j,isw} \cdot pen_1 \cdot \frac{etat_{i,j}}{dzt_1} \quad (5)$$

$$- sbcocn_{i,j,isw} \cdot pen_{kmt_{i,j}-1} \cdot \frac{zw_{kmt_{i,j}} - ht_{i,j}}{dzt_{kmt_{i,j}}}$$

$$- sbcocn_{i,j,isw} \cdot pen_{kmt_{i,j}} \cdot \frac{dht_{i,kmt_{i,j},j}}{dzt_{kmt_{i,j}}}.$$

This integral represents the net internal heating/cooling of the water column in response to the divergence of penetrative shortwave flux, and it must be zero because $pen_0 = 0$. In other words, the shortwave penetration scheme is intended to act as vertical redistributor of the shortwave component of the surface heat flux, and the total heating of the second and deeper layers must be compensated for by the cooling of the first layer. However, the first term acts as an artificial heat sink (source) at the region with positive (negative) $etat_{i,j}$, and the second term acts as an artificial heat sink everywhere as long as the partial bottom cell is used ($ht_{i,j} \le zw_{kmt_{i,j}}$). These two terms arise from dzt_k being used rather than $dht_{i,k,j}$ as a denominator in the r.h.s. of Eq. (2), referred to here as "the first problem." The third term in the r.h.s. of Eq. (5) implies that shortwave irradiance penetrates the ocean bottom and acts as an artificial heat sink everywhere. We call

this "the second problem," and this problem can be overcome by using land–sea mask $tmask_{i,k,j}$ (zero for a land cell and one for an ocean cell) for a numerator in the r.h.s. of Eq. (2). In conclusion, Eq. (2) must be modified to exclude artificial heat sources and sinks as

$$divpen_{i,k,j} = \frac{pen_{k-1} - pen_k \cdot tmask_{i,k+1,j}}{dht_{i,k,j}} \quad (k=1,...,km). \quad (6)$$

Additionally, we modify the penetration ratio pen_k to incorporate the contribution of spatiotemporal variations of $etat_{i,j}$ by replacing zw_k, the bottom depth of the k-th cell from a fixed reference level, with $etat_{i,j} + zw_k$, the bottom depth from the sea surface:

$$pen'_{i,k,j} = A \cdot e^{-(etat_{i,j}+zw_k)/l_1} + (1-A) \cdot e^{-(etat_{i,j}+zw_k)/l_2} \quad (7a)$$

$$\approx e^{-etat_{i,j}/l_2} \cdot pen_k \quad (k=1,...,km), \quad (7b)$$

where we neglect the first term in the r.h.s. of Eq. (7a) because we usually set the surface cell thickness zw_1 to be greater than 5 m, which is already much greater than $l_1 = 0.35$ m, and approximate the ratio in the final form (7b) for computational efficiency by
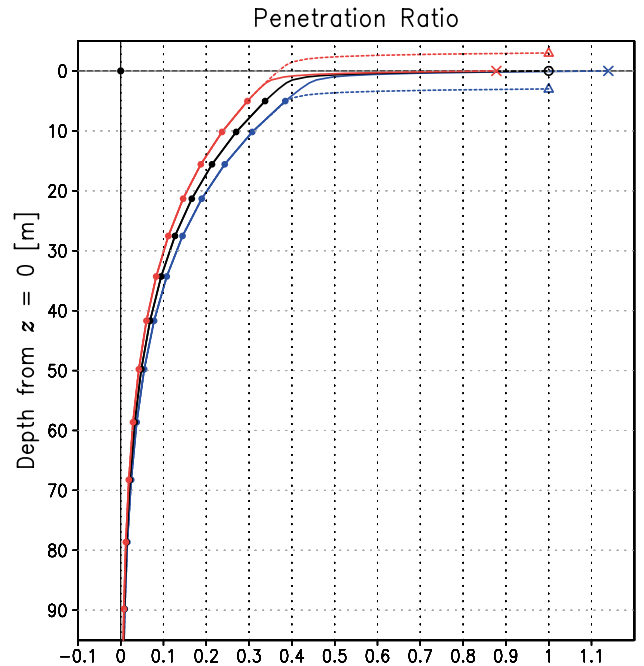
Fig. 2. Vertical profiles of the shortwave penetration ratios. The black line indicates the original ratio pen_k defined by Eq. (1), whereas the red and blue solid lines indicate the modified ratios $pen'_{i,k,j}$ defined by Eq. (7b) for the cases of $etat_{i,j} = +3$ m and $etat_{i,j} = -3$ m, respectively. The red and blue dotted lines indicate the modified ratios $pen'_{i,k,j}$ without the approximation defined by Eq. (7a). The closed circles represent the ratios at zw_k, the bottom depth of the vertical k-th cell from a fixed reference level ($z = 0$), used in this report.

multiplying the original penetration ratio pen_k (vertical structure) by the factor $e^{-etat_{i,j}/l_2}$ (horizontal structure). We only need to calculate the latter factor for every time step at every horizontal grid point instead of performing a three-dimensional calculation of $pen'_{i,k,j}$ in the strict form. The vertical profiles of the modified ratio for the cases of $etat_{i,j} = \pm 3$ m are shown in Fig. 2 (red and blue lines). The solid lines are modified ratios defined by Eq. (7b) and hypothetically equal to $e^{-etat_{i,j}/l_2}$ at $zw = 0$ (crosses), whereas the dotted lines are those without approximations defined by Eq. (7a) and hypothetically equal to one at $zw = -etat_{i,j}$ (open triangles). The former ratios closely approximate the latter for $k \geq 1$. In these cases, the original and modified penetration ratios (and hence their divergences) differ by more than 10%. This modification causes systematic subsurface cooling in the subtropics, where $etat_{i,j}$ is generally positive. The magnitude of this cooling, however, is on the order of hundredths of a °C at about the 10th model year and is much smaller than the changes induced by the first and second problems. Therefore, we focus on the latter two problems in this report.

3. Experiments

The latest version of OFES already contains all the modifications described above and $divpen_{i,k,j}$ is evaluated as

$$divpen_{i,k,j} = \frac{pen'_{i,k-1,j} - pen'_{i,k,j} \cdot tmask_{i,k+1,j}}{dht_{i,k,j}} \quad (k = 1,...,km), \quad (8)$$

where $pen'_{i,k,j}$ is defined by Eq. (7b). This is used for reference simulation, and we call it the CTL run. To assess the effects from the first and second problems separately, two experimental simulations are carried out as follows.

In the first case, the first problem remains unsolved, and $divpen_{i,k,j}$ is evaluated as

$$divpen_{i,k,j} = \frac{pen_{k-1} - pen_k \cdot tmask_{i,k+1,j}}{dzt_k} \quad (k = 1,...,km), \quad (9)$$

that is, dzt_k is used instead of $dht_{i,k,j}$ as a denominator. In addition, pen_k is evaluated by Eq. (1) rather than by Eq. (7b). We call this simulation the SFC run, although it contains deficiencies caused by both the free surface and the partial bottom cell.

In the second case, the second problem remains unsolved, and $divpen_{i,k,j}$ is evaluated as

$$divpen_{i,k,j} = \frac{pen'_{i,k-1,j} - pen'_{i,k,j}}{dht_{i,k,j}} \quad (k = 1,...,km), \quad (10)$$

that is, $tmask_{i,k+1,j}$ is not used for a numerator, and the shortwave irradiance penetrates the ocean bottom. We call this simulation the BTM run.

Except for the shortwave penetration scheme, the CTL, SFC, and BTM runs share a common setting. The model domain covers the entire globe, and the ocean model is coupled with a sea-ice model (Komori et al., 2005). The horizontal resolution is 1/2 ° in the directions of both longitude and latitude. It contains 54 levels in the vertical, with varying cell thicknesses from $dzt_1 = 5$ m at the surface to $dzt_{54} = 330$ m at the maximum depth of 6,065 m, as in the eddy-resolving version of OFES (Masumoto et al., 2004; Sasaki et al., 2006, 2008). The minimum of $kmt_{i,j}$ is set to 3, and the minimum of $ht_{i,j}$ is 15.2 m, which is slightly less than $zw_3 = 15.6$ m because the partial bottom cell is considered.

Figure 3 shows the ocean depth $ht_{i,j}$ used in this report. The penetration ratio at the ocean bottom pen_{btm}, which will be described in the next section, is calculated with $ht_{i,j}$ by

$$pen_{btm} = A \cdot e^{-ht_{i,j}/l_1} + (1-A) \cdot e^{-ht_{i,j}/l_2}. \quad (11)$$

We assume that $etat_{i,j} = 0$ here for simplicity. The spatial distribution of pen_{btm} is shown in Fig. 4. The ratio exceeds 15% in shallow coastal areas and is over 20% at some points.

The initial conditions are taken from climatological temperature and salinity fields for January in the World Ocean Atlas 2005 (WOA05; Locarnini et al., 2006; Antonov et al., 2006) with no motion and no sea ice. The surface boundary conditions are taken from Common Ocean-ice Reference Experiments (CORE; Large and Yeager, 2004, 2009) Corrected Normal Year Forcing version 2, whereas the sea surface salinity is restored to the climatological monthly salinity of WOA05 with a time constant of 30 days. Note that freshwater flux, instead of salt flux, is applied as a surface boundary condition differently from the eddy-resolving version of OFES, in which no sea-ice model is coupled. For each run, 25 years of integration are conducted, and monthly mean outputs are stored. The results are analyzed focusing primarily on their annual-mean fields.
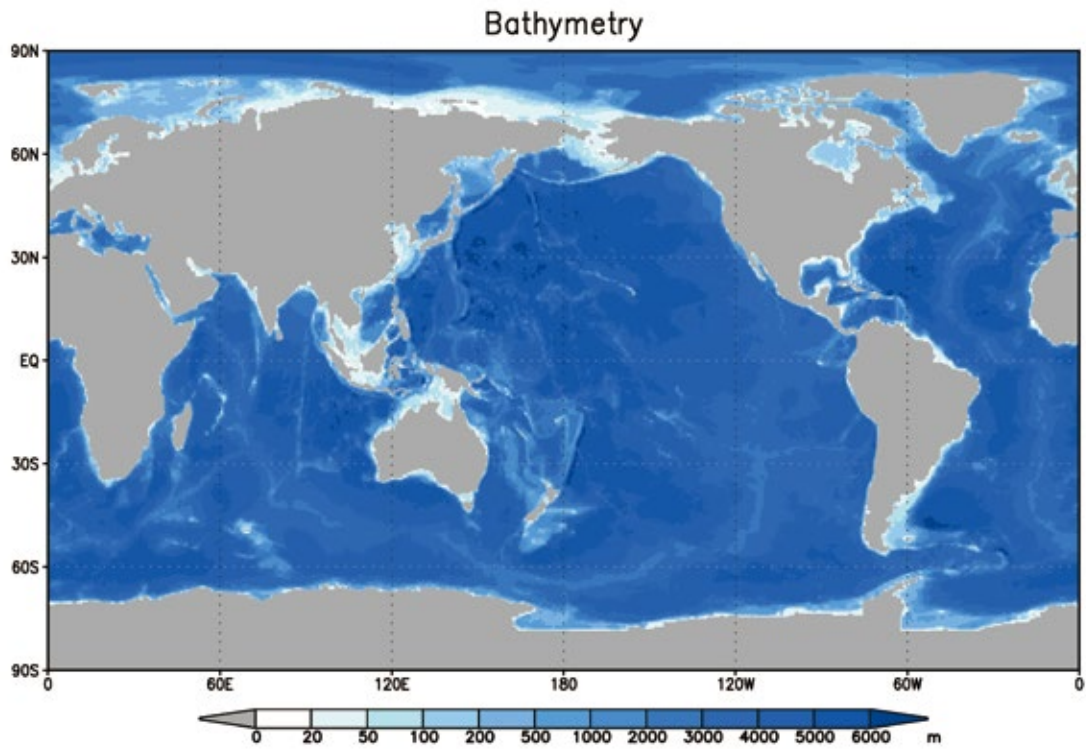
Bathymetry

Fig. 3.   Model bathymetry [m].

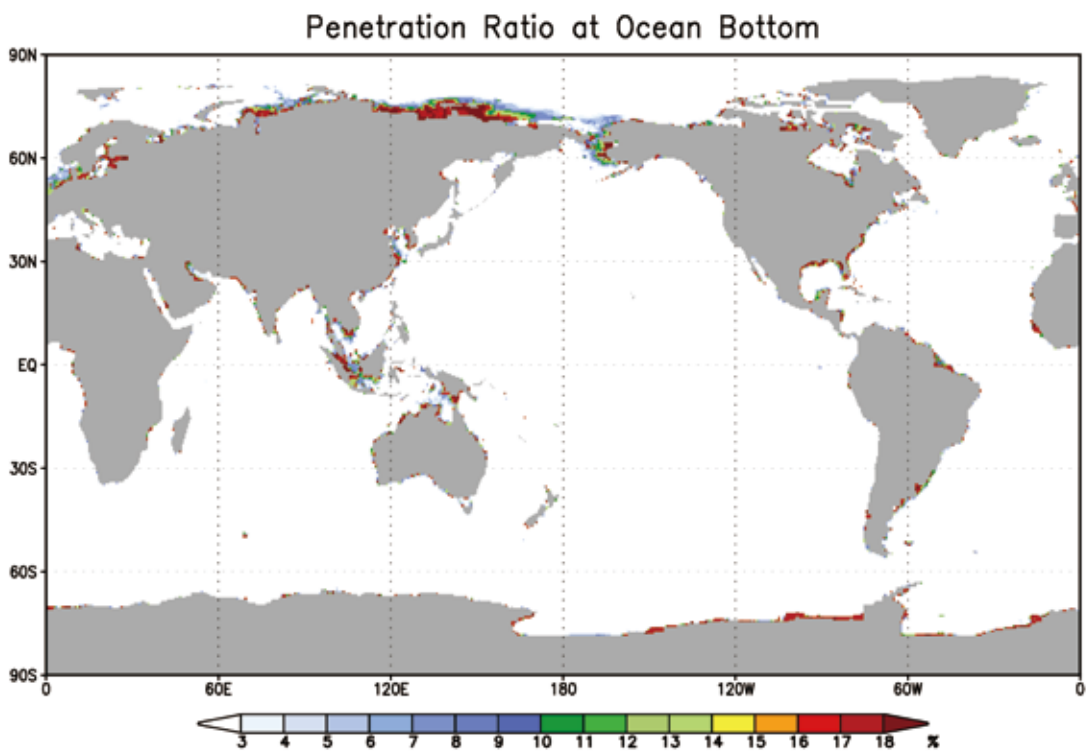## Penetration Ratio at Ocean Bottom

Fig. 4.   The shortwave penetration ratio at the ocean bottom pen_{btm} [%].

4. Results

4.1. The temporal change in global-mean fields

Figure 5 shows 25-year time series of global mean sea surface temperature (SST), downward latent heat flux (LHF), and sea level (including the contribution from sea ice and snow as well as from SSH) for each run. As noted in the previous section, the surface boundary conditions have no interannual variability.

During the initial 4 or 5 years, each run changes similarly, with an increase in SST (Fig. 5a), a decrease in downward LHF (equivalent to an increase in evaporation, Fig. 5b), and an increase in sea level (Fig. 5c). After the initial 4 or 5 years, both CTL and BTM runs still have weak increasing and decreasing trends in SST and downward LHF, respectively, whereas these runs exhibit a weak decreasing trend in sea level. The SFC run has opposite trends to those of the CTL and BTM runs, and their differences increase exponentially with time. This point will be discussed later.

4.2. Estimating artificial heat sources and sinks

Artificial heat sources and sinks caused by the first and second problems are estimated on the basis of the monthly output of the CTL run. The sources and sinks are averaged over the final 5 years (from the 21st through the 25th model years) to smooth out mesoscale variability.

The annual-mean field of the term $-sbcocn_{i,j,isw} \cdot pen_1 \cdot etat_{i,j}/dzt_1$ in Eq. (5) is shown in Fig. 6. The annual-mean SSH $etat_{i,j}$ is also plotted in the figure. As described in section 2, positive (negative) areas of $etat_{i,j}$ correspond to regions of artificial heat sinks (sources) when the problem is not solved. The term is negative over the tropics and subtropics, especially in the Pacific and Indian Oceans, whereas it is positive over the subpolar regions and the Southern Ocean. The magnitude exceeds 13 W m^{-2} at about 15 °N in the western North Pacific, where SSH has its maximum, and reaches 10 W m^{-2} over the subpolar gyre in the North Atlantic and over the Southern Ocean.

Shortwave flux penetrating the ocean bottom is estimated by multiplying the shortwave surface boundary condition $sbcocn_{i,j,isw}$ and the penetration ratio at the ocean bottom pen_{btm} (Fig. 4) defined by Eq. (11). The annual-mean field of $-sbcocn_{i,j,isw} \cdot pen_{btm}$ is displayed in Fig. 7. Although the large negative value of the term is restricted within shallow coastal areas, as expected, the magnitude exceeds 50 W m^{-2} in regions such as the Indonesian archipelago and the mouth of the Amazon River. Note that the extent of the simulated summer sea-ice in the Arctic Ocean is overestimated (not shown). This may cause the bottom flux to remain small off the coast of East Siberia in spite of a high pen_{btm} in that region because sea ice reflects a large portion
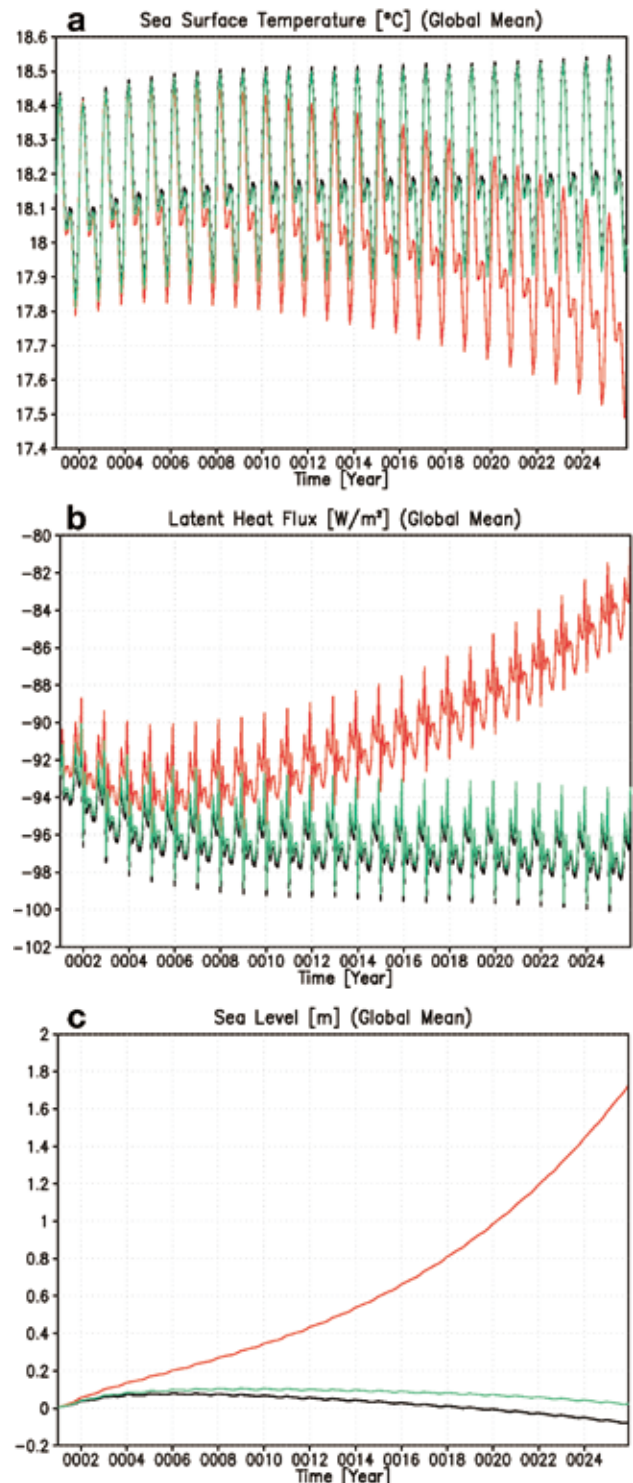

Fig. 5. A time series of the global mean (a) sea surface temperature [°C], (b) downward latent heat flux [W m^{-2}], and (c) sea level [m] calculated from the (black) CTL, (red) SFC, and (green) BTM runs.

$-sbcocn_{isw} \times pen_1 \times \eta / \Delta z_1$ (CTL, Annual Mean, 0021−0025)
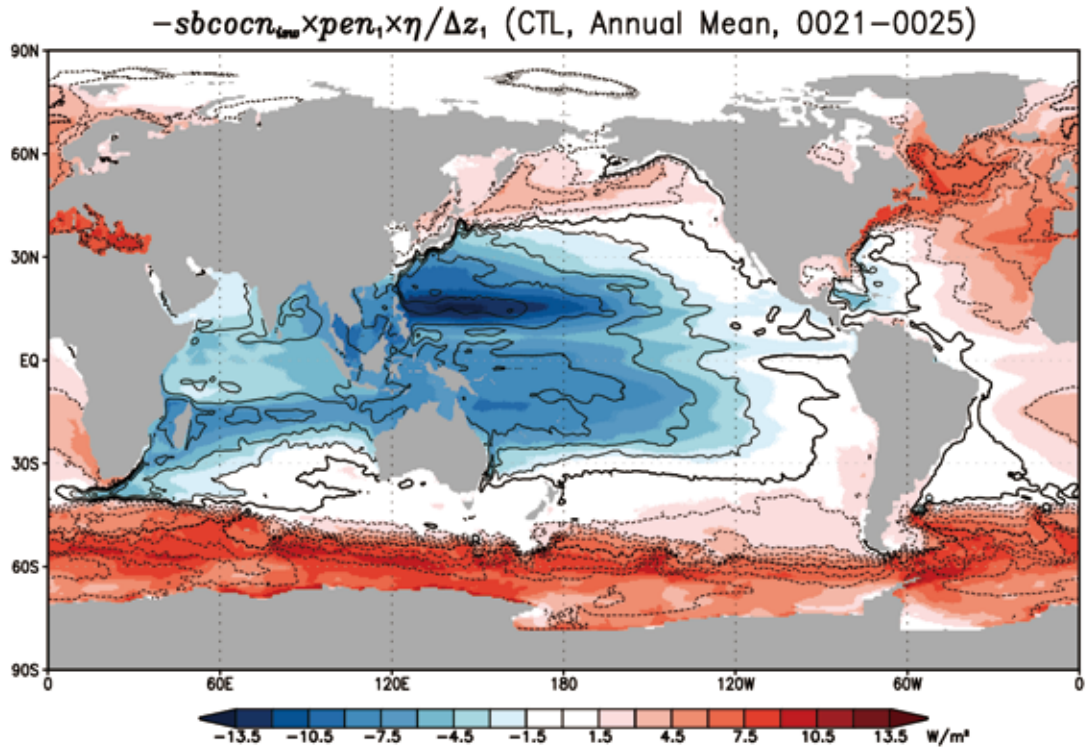

Fig. 6. The annual-mean field of $-sbcocn_{i,j,isw} \cdot pen_1 \cdot etat_{i,j}/dzt_1$ [W m^{-2}] evaluated on the basis of the monthly output of the CTL run. The sea surface height $etat_{i,j}$ is also plotted in contours, and the interval is 20 cm.
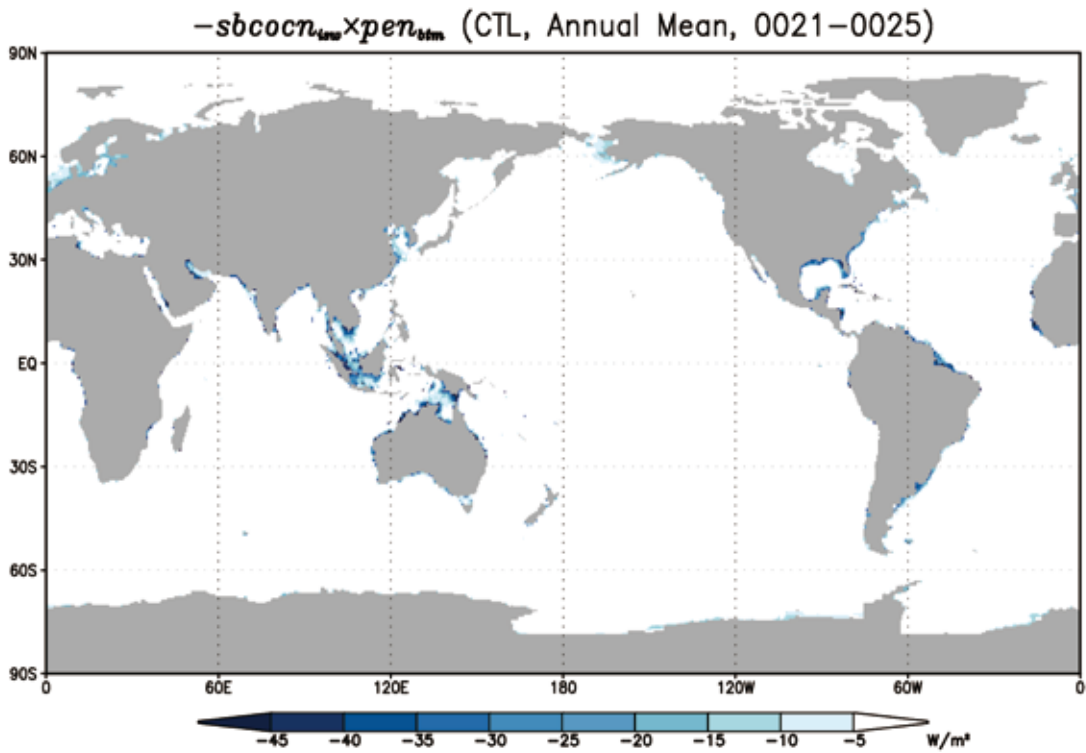
$-sbcocn_{isw} \times pen_{btm}$ (CTL, Annual Mean, 0021−0025)

Fig. 7. The annual-mean field of $-sbcocn_{i,j,isw} \cdot pen_{btm}$ [W m^{-2}] evaluated on the basis of the monthly output of the CTL run.

of the shortwave flux at the ocean surface.

Amplitudes of both $-sbcocn_{i,j,isw} \cdot pen_1 \cdot etat_{i,j} / dzt_1$ and $-sbcocn_{i,j,isw} \cdot pen_{btm}$ have clear seasonality accompanied by the meridional migration of the surface shortwave flux: the amplitude in the summer hemisphere is much larger than that in the winter hemisphere (not shown). As a result, the estimated artificial heat source/sink in the summer hemisphere is much greater than that on the basis of the annual mean described above.

4.3. Comparisons involving the CTL run

As seen in Section 4.1, the difference between SFC and CTL/BTM runs grows exponentially after about the 5th model year (Fig. 5). We compare the results of the 5th model year to distinguish the direct effects of modifications in a shortwave penetration scheme from the consequences through feedback processes.

4.3.1. The SFC run

Figure 8 shows an annual mean difference in SST between the SFC and CTL runs (a deviation of the SFC run from the CTL run). The SST of the SFC run is lower than that of the CTL run over the tropics and subtropics in the Pacific and Indian Oceans and higher over the subpolar regions in the Pacific and Atlantic Oceans and over the Southern Ocean. This result is in close correspondence with the estimated distribution of the annual mean artificial heat source/sink resulting from the first problem ($-sbcocn_{i,j,isw} \cdot pen_1 \cdot etat_{i,j}/dzt_1$, Fig. 6). The maximum amplitude of the difference in SST is approximately 0.3 °C except for differences induced by mesoscale variability around the SST fronts associated with the western boundary currents and the Antarctic Circumpolar Current.

This difference in temperature is not confined within the uppermost layer but extends to the subsurface through a vertical mixing process. Figure 9 shows meridional–vertical sections of the annual mean temperature difference between the SFC and CTL runs
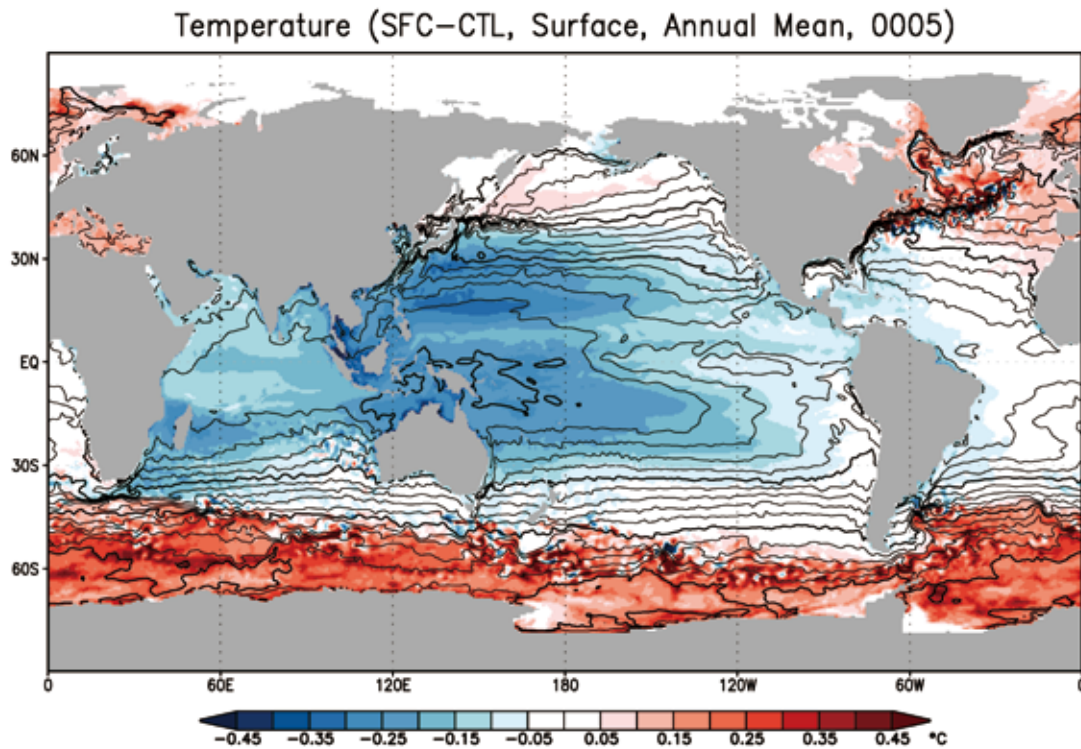

Fig. 8. The annual mean difference in sea surface temperature [°C] between the SFC and CTL runs (SFC − CTL). The sea surface temperature of the CTL run is also plotted in contours, and the interval is 2°C.

in the Indian (along 60°E, Fig. 9a), Pacific (along 160°E, Fig. 9b), and Atlantic Oceans (along 40°W, Fig. 9c). The positive temperature difference in the subpolar regions of these oceans extends up to the 50–100 m depth, and the negative difference in the subtropics of the Pacific reaches a much deeper layer, especially in the region where a thick mixed layer is formed in late winter (e.g., at about 30°N in Fig. 9b). Note that high temperature differences on the polar sides of 40° result from the mesoscale variability mentioned above.

Because the prescribed surface atmospheric variables, such as surface air temperature and humidity, are the same between the SFC and CTL runs, the difference in SST leads to a difference in turbulent (sensible and latent) heat fluxes as well as the upward longwave radiation flux. The annual-mean difference in downward net heat flux (Fig. 10) is positive (negative) where the SST difference (Fig. 8) is negative (positive), and the artificial heat source/sink resulting from the first problem is partially compensated by this anomalous heat flux. That is, this process provides negative feedback.

With regard to the global-mean fields, however, the decrease in evaporation caused by the decrease in SST induces an increase in sea level because the amounts of precipitation and river runoff are "corrected" to almost balance the estimated evaporation and are fixed in these simulations with a stand-alone OGCM. The increase in sea level, in turn, enhances the artificial heat sink resulting from the first problem, which is proportional to SSH $etat_{i,j}$. This positive feedback explains the exponential growth of the difference between the SFC and CTL runs (Fig. 5). Note that in cases of coupled atmosphere–ocean simulations, a decrease in evaporation usually leads to a decrease in precipitation, and the positive feedback may not exist. Additionally, in cases of stand-alone ocean simulations forced by surface salt flux, as in the cases with the eddy-resolving version of OFES (Masumoto et al., 2004; Sasaki et al., 2006, 2008), the amount of evaporation/precipitation does not affect SSH; thus, the positive feedback does not exist.

4.3.2. The BTM run

Figure 11 shows the annual mean difference in SST between the BTM and CTL runs (the deviation of the BTM run from the CTL run). As expected from the estimated distribution of the annual mean artificial heat sink resulting from the second problem ($-sbcocn_{i,j,isw} \cdot pen_{btm}$, Fig. 7) the SST of the BTM run is much lower than that of the SFC run within shallow coastal areas, and the magnitude exceeds 1.0°C in some regions. In cases of coupled atmosphere–ocean simulations, such a large difference in the SST, particularly over warm water pool around the Indonesian archipelago, may affect large-scale atmospheric circulation through
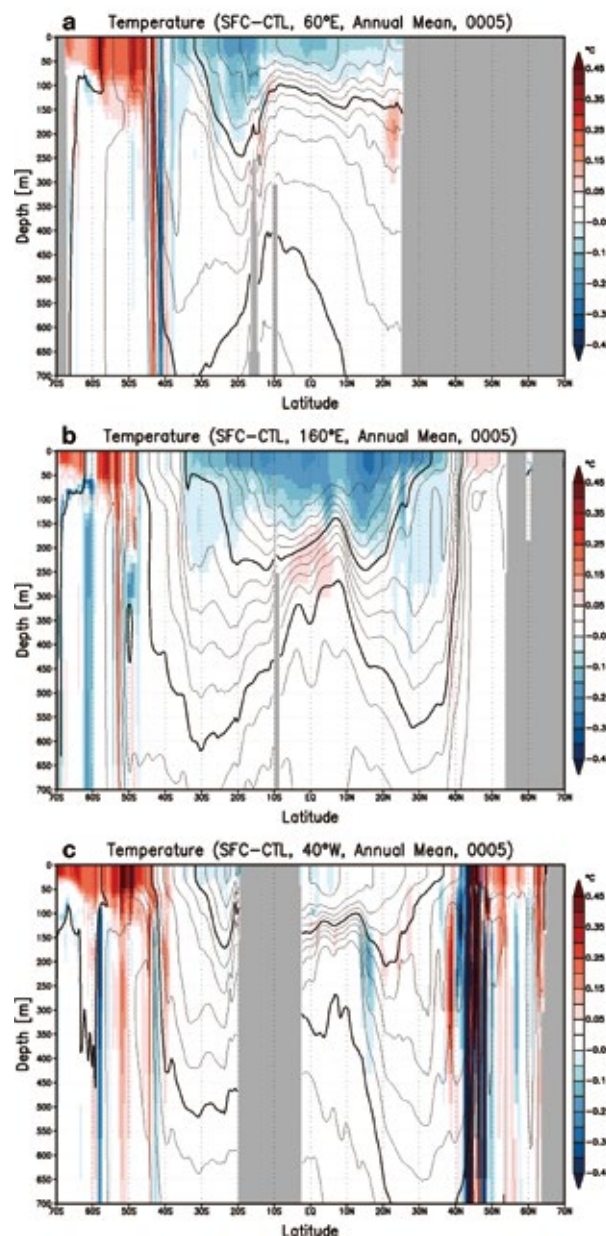

Fig. 9.   The annual mean difference in temperature [°C] between the SFC and CTL runs (SFC − CTL) along (a) 60°E, (b) 160°E, and (c) 40°W. The temperatures of the CTL run are also plotted in contours, and the interval is 2°C.
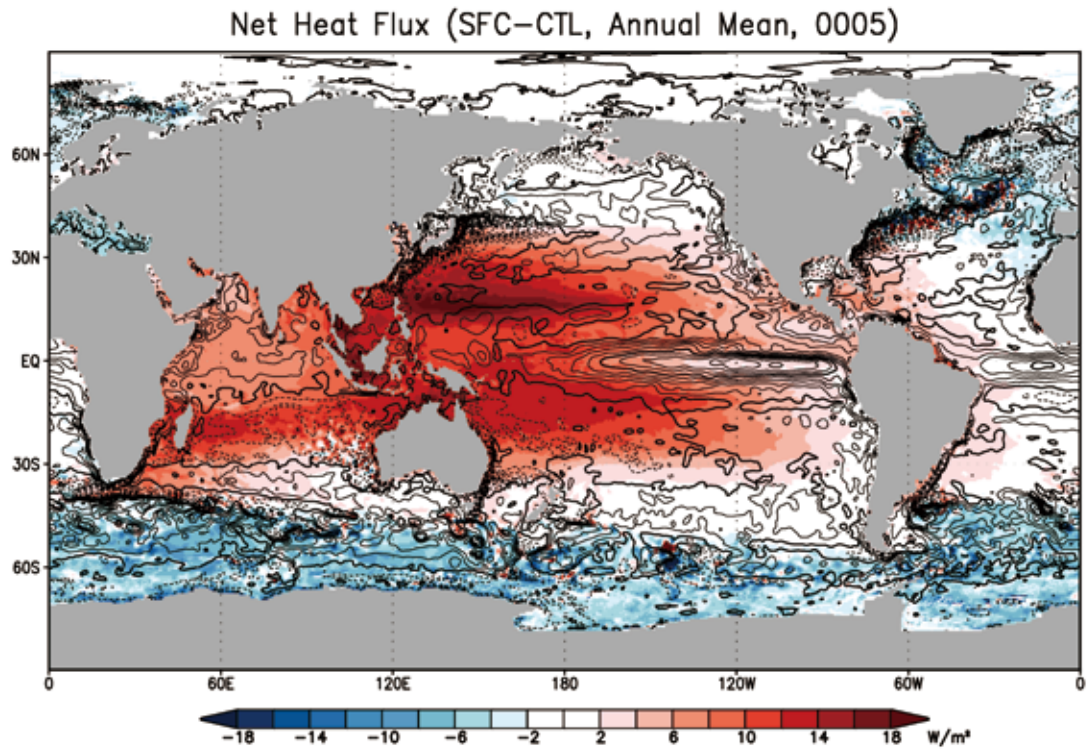
Net Heat Flux (SFC−CTL, Annual Mean, 0005)

Fig. 10. The same as in Fig. 8 but for the downward net heat flux [W m^{-2}]. The contour interval is 2 W m^{-2}.
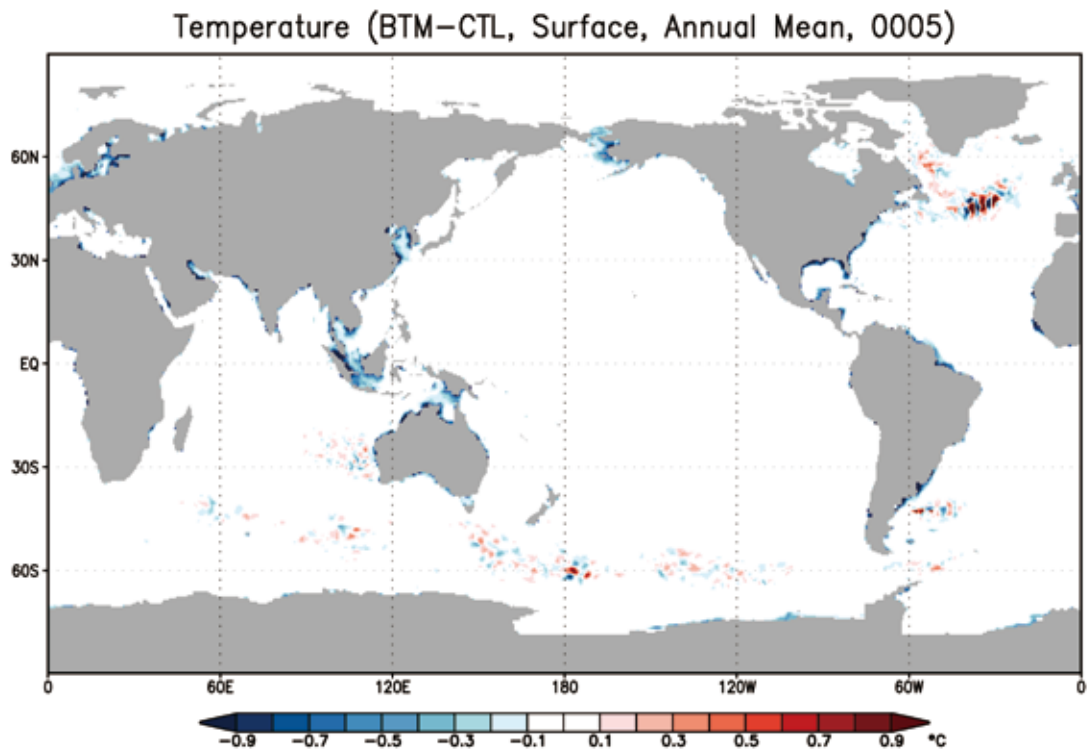
Temperature (BTM−CTL, Surface, Annual Mean, 0005)

Fig. 11. The annual mean difference in sea surface temperature [°C] between the BTM and CTL runs (BTM − CTL).

convective processes (e.g., McPhaden and Picaut, 1990; Webster and Lukas, 1992).

Again, the decrease in SST leads to an increase in the downward net heat flux (Fig. 12). In this case, the artificial heat sink through the ocean bottom resulting from the second problem (Fig. 7) seems to be locally balanced with this anomalous surface heat flux, and neither the distribution nor the amplitude of the annual mean difference in SST between the BTM and CTL runs change substantially even in the latter period of the 25-year integration (not shown). Thus, the global mean differences between the BTM and CTL runs in SST (Fig. 5a) and in downward latent heat flux (Fig. 5b) are kept almost constant (approximately $-0.013°C$ and $+0.33$ $W\,m^{-2}$, respectively) throughout the integration period, whereas the difference in sea level (Fig. 5c) grows linearly (approximately $4 \times 10^{-3}\,m\,year^{-1}$).

5. Concluding remarks

Two problems with the shortwave penetration scheme used in MOM3 are assessed by stand-alone ocean simulations using a MOM3-based OGCM (OFES). The first problem arises from a fixed layer thickness dzt_k being used rather than variable thickness $dht_{i,k,j}$ in the scheme and causes an artificial heat sink (source) at the region with positive (negative) SSH $etat_{i,j}$. As a result, a low SST bias is produced over the tropics and subtropics in the Pacific and Indian Oceans, and a high SST bias is produced over the subpolar regions in the Pacific and Atlantic Oceans and over the Southern Ocean. These biases extend to the subsurface through a vertical mixing process. The second problem is that shortwave irradiance penetrates the ocean bottom. This induces a large artificial heat sink and a significantly low SST bias, but both are restricted within shallow coastal areas.

As mentioned above, it is necessary to prevent shortwave irradiance from penetrating the ocean bottom in order to conserve the heat. Such a treatment, however, can lead to an excess heating of the bottom cell in some areas as a result of the convergence of shortwave flux. Convective instability is expected to occur to mix the water column vertically, but intense haline stratification can prohibit the instability, for instance, at the mouths of large rivers such as the Amazon River (not shown). A more effective treatment of shortwave flux, e.g., the reflection at the ocean bottom and upward repenetration or the introduction of water turbidity, may be required to overcome this problem, but these adjustments are beyond the scope of this report.

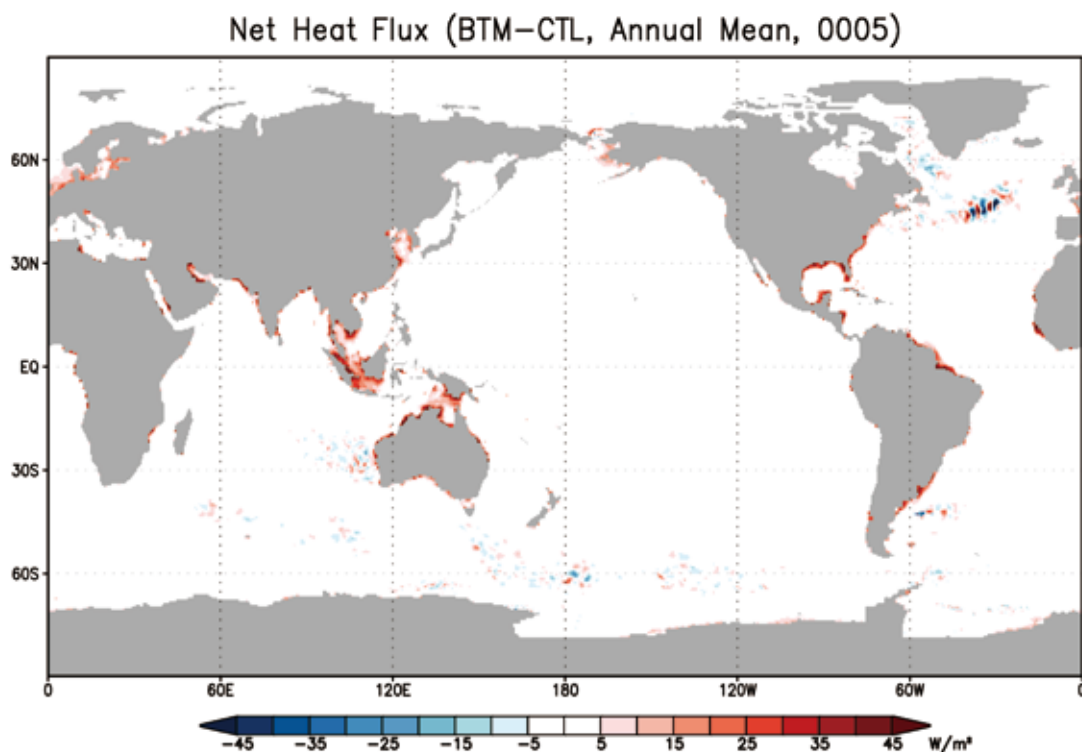In this report, we used a climatological forcing instead

Fig. 12.   The same as in Fig. 11 but for the downward net heat flux [$W\,m^{-2}$].

of an interannually varying forcing for simplicity. Because some interannual phenomena, such as the El Niño–Southern Oscillation, are accompanied by changes in SSH, our modification of the shortwave penetration scheme may contribute to a more realistic reproducibility of such phenomena in ocean and coupled atmosphere–ocean simulations using MOM3 and MOM3-based OGCMs.

References

Antonov, J. I., R. A. Locarnini, T. P. Boyer, A. V. Mishonov, and H. E. Garcia (2006), World Ocean Atlas 2005, Volume 2: Salinity, NOAA Atlas NESDIS 62, U.S. Government Printing Office, 182 pp.

Griffies, S. M. (2007), Elements of MOM4p1, GFDL Ocean Group Technical Report No. 6, NOAA/Geophysical Fluid Dynamics Laboratory.

Griffies, S. M., M. J. Harrison, R. C. Pacanowski, and A. Rosati (2004), A Technical Guide to MOM4, GFDL Ocean Group Technical Report No. 5, NOAA/Geophysical Fluid Dynamics Laboratory.

Jerlov, N. G. (1976), Marine Optics, Elsevier, 231 pp.

Komori, N., K. Takahashi, K. Komine, T. Motoi, X. Zhang, and G. Sagawa (2005), Description of sea-ice component of Coupled Ocean–Sea-Ice Model for the Earth Simulator (OIFES), *J. Earth Simulator*, *4*, 31–45.

Large, W. G. and S. G. Yeager (2004), Diurnal to decadal global forcing for ocean and sea-ice models: the data sets and flux climatologies, NCAR Technical Note NCAR/TN-460+STR, Climate and Global Dynamics Division of the National Center for Atmospheric Research.

Large, W. G. and S. G. Yeager (2009), The global climatology of an interannually varying air–sea flux data set, *Climate Dyn.*, *33*, 341–364, doi:10.1007/s00382-008-0441-3.

Locarnini, R. A., A. V. Mishonov, J. I. Antonov, T. P. Boyer, and H. E. Garcia (2006), World Ocean Atlas 2005, Volume 1: Temperature, NOAA Atlas NESDIS 61, U.S. Government Printing Office, 182 pp.

Masumoto, Y., H. Sasaki, T. Kagimoto, N. Komori, A. Ishida, Y. Sasai, T. Miyama, T. Motoi, H. Mitsudera, K. Takahashi, H. Sakuma, and T. Yamagata (2004), A fifty-year eddy-resolving simulation of the world ocean—Preliminary outcomes of OFES (OGCM for the Earth Simulator), *J. Earth Simulator, 1*, 35–56.

McPhaden, M. J. and J. Picaut (1990), El Niño–Southern Oscillation displacements of the western equatorial Pacific warm pool, *Science, 250*, 1385–1388, doi: 10.1126/science.250.4986.1385.

Pacanowski, R. C. and S. M. Griffies (1999), MOM 3.0 Manual, GFDL Ocean Group Technical Report No. 4, NOAA/Geophysical Fluid Dynamics Laboratory.

Paulson, C. A. and J. J. Simpson (1977), Irradiance measurements in the upper ocean, *J. Phys. Oceanogr., 7*, 952–956.

Sasaki, H., M. Nonaka, Y. Masumoto, Y. Sasai, H. Uehara, and H. Sakuma (2008), chap. 10 An eddy-resolving hindcast simulation of the quasiglobal ocean from 1950 to 2003 on the Earth Simulator, K. Hamilton and W. Ohfuchi (eds.), High Resolution Numerical Modelling of the Atmosphere and Ocean, Springer, 157–185.

Sasaki, H., Y. Sasai, M. Nonaka, Y. Masumoto, and S. Kawahara (2006), An eddy-resolving simulation of the quasi-global ocean driven by satellite-observed wind field: Preliminary outcomes from physical and biological fields, *J. Earth Simulator, 6*, 35–49.

Webster, P. J. and R. Lukas (1992), TOGA COARE: The Coupled Ocean–Atmosphere Response Experiment, *Bull. Amer. Meteorol. Soc., 73*, 1377–1416.